Multicomponent ambient seismic noise correlations at Valhall: Characterization and correlation of microseism noise in the ambient seismic field

Sjoerd de Ridder

ABSTRACT

The basis for successful application of passive seismic interferometry depends on the characteristic of the ambient noise. This paper introduces four continuous recordings made at the Valhall Life of Field Seismic (LOFS) Array. The ambient seismic field is characterized through creation and analysis of various spectra, focusing particularly on the microseism energy between 0.175 and 1.75 Hz. Beam forming shows how the microseism noise is generally incident equally strongly from all directions for long periods of time, with certain exceptions. Finally, seismic interferometry is used to create virtual seismic sources for all receivers at Valhall. By cross-correlating different components at different stations, I retrieve a full virtual seismic Green's matrix that reveals interface waves of Scholte and Love wave types. A first overtone of Scholte is observed as well.

INTRODUCTION

At Valhall in the Norwegian North Sea, a permanent recording array was installed in 2003 (Kommedal et al., 2004) for repeated active seismic surveying. This array, named the Life of Field Seismic (LOFS) array, has the capability to record continuously under a variety of circumstances. Conventional active seismic surveying provides highly detailed subsurface images, but at only at a few snapshots in time. Passive seismic interferometry creates virtual seismic sources from ambient noise (Wapenaar, 2004), thus providing a means to survey the subsurface continuously. Since the subsurface at Valhall is well known from active seismic (Barkved and Kristiansen, 2005; Sirgue et al., 2010), recordings made by the LOFS array provide an good opportunity to study the ambient seismic field and the application of seismic interferometry at a reservoir scale.

The quality of virtual seismic sources obtained from passive seismic interferometry depends on the characteristic of the ambient noise. Firstly, noise can be characterized by its spatially and temporally varying time-frequency spectrum. Secondly, the propagation direction of the waves composing the ambient field can be studied using beam forming experiments. Finally, I perform seismic interferometry and create virtual seismic sources for all receivers at Valhall. Cross-correlating different compo-

nents at different stations retrieves a full virtual seismic Green's matrix. I finish with a modal analysis of the components of the virtual seismic Green's matrix.

NOISE RECORDINGS OF THE AMBIENT SEISMIC FIELD AT VALHALL

The LOFS installation has been in place since 2003 and can record continuously, but recordings are usually only permanently stored when controlled source seismic surveys are acquired. Artman (2006) suggested that several long and continuous recordings be stored and studied at frequencies above 2 Hz with the aim of passive imaging by seismic interferometry. Artman (2006) acquired two recordings:

- February 13$^{\text{th}}$, 2004: 29 hours, 29 minutes and 16 seconds starting UT 14:14:14.
- January 19$^{\text{th}}$, 2005: 6 hours, 39 minutes and 30 seconds starting UT 19:35:45.

Unfortunately, retrieving virtual seismic sources at higher frequencies by seismic interferometry is not straightforward. Later work by Dellinger (2008) revealed that seismic interferometry applied at frequencies below 2 Hz results in high quality virtual seismic Scholte-wave sources. This spurred the decision to remove the standard-acquisition low-cut filter and record while the remnants of tropical storm Laura moved over the North Sea generating ambient data rich in low frequencies.

- October 4$^{\text{th}}$, 2008: 2 hours starting at UT 14:11:24.

Finally a much longer recording was stored, again without low-cut filter, and made available for this study.

- December 22$^{\text{nd}}$, 2010: 5 days, 1 hour, 47 minutes and 20 seconds starting UT 21:16:39.

The recordings of 2004, 2005 and 2008 were made with a sampling rate of 250 samples per second, and the 2010 recording was made with 500 samples per second.

Figure 1 shows time slices of the data recorded in the vertical component of the geophone, after bandpasses conducted in the frequency domain with a Hann taper. At the lowest frequencies, $0.25 - 0.35$ Hz, we find an incoherent random wave field, known as microseism energy, that is not spatially aliased at the very low frequencies but spatially aliased at higher frequencies, $1.0 - 1.5$ Hz, as seen in Figure 1b. Figure 1c shows ample energy, between $5 - 10$ Hz, radiating from platforms installed at Valhall fields. At even higher frequencies, $15 - 25$ Hz in Figure 1d, we find almost planar wave fields incident from the direction of Ekofisk fields, and potentially originating there. They are found at intervals of 10 seconds, which is a regular interval for seismic shooting. All four time-slices are extracted at UT 0:17:00 December 24$^{\text{th}}$, 2010.

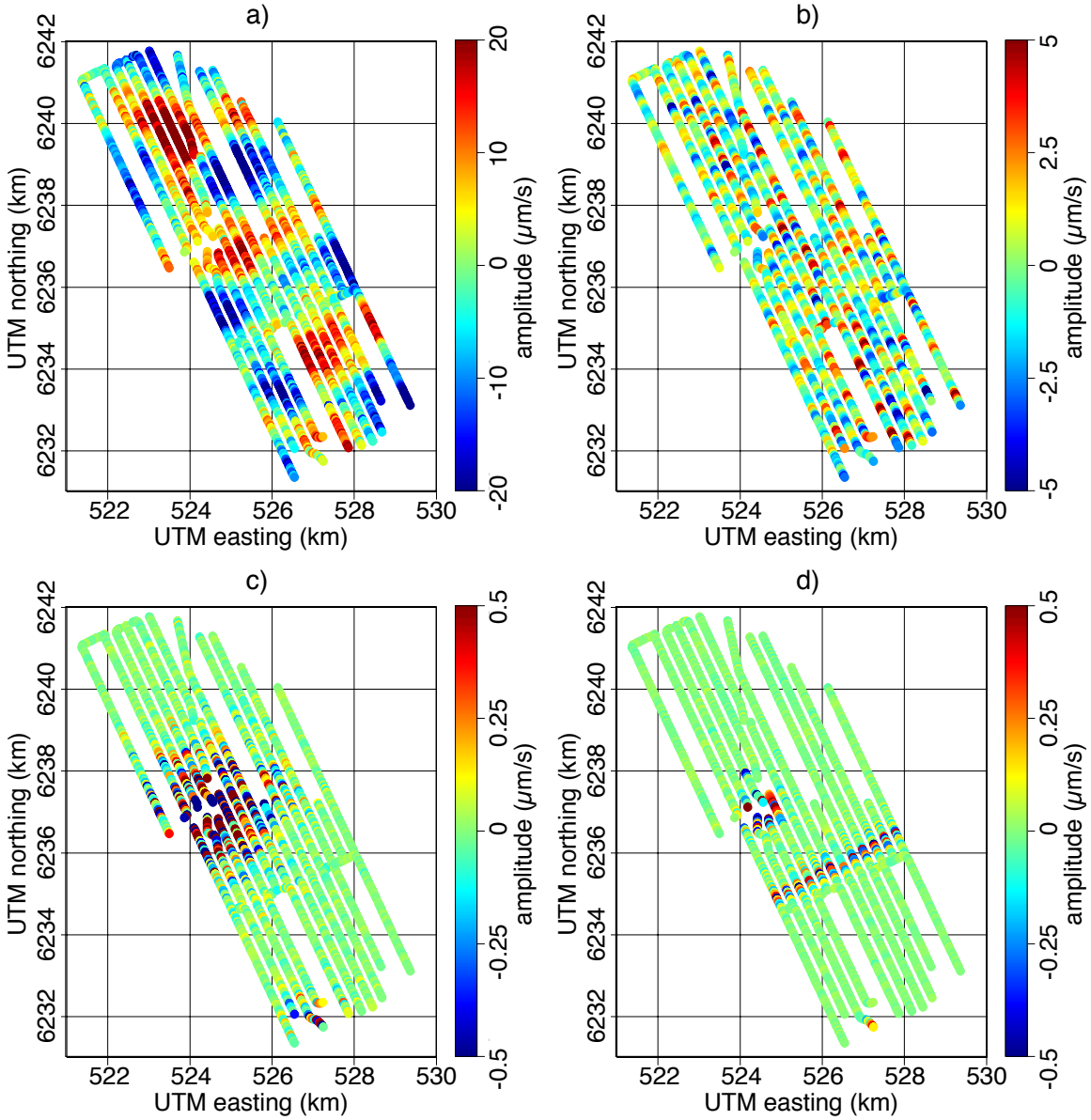

Figure 1: Amplitude maps extracted at UT 0:17:00 December 24$^{\text{th}}$, 2010. a) $0.25 - 0.35$ Hz, b) $1.0 - 1.5$ Hz, c) $5 - 10$ Hz, d) $15 - 25$ Hz. [**CR**]

Frequency spectra as function of space

One way of characterizing the ambient seismic field is by investigating how the spectrum changes over space (McNamara and Boaz, 2005). A three hour continuous block of data was selected from the 2010 data (starting UT 0:17:18) during a period when the active seismic shots were silent (see next section). These 3 hours were divided into 2.5-minute windows with 50% overlap. The time-frequency spectrum was computed for each time-window and averaged over all time windows. Figure 2 contains 9 maps for frequencies $10^{-\frac{2}{3}}$, $10^{-\frac{1}{3}}$, $10^{0}, 10^{\frac{1}{3}}$, $10^{\frac{2}{3}}$, $10^{1\frac{1}{3}}$, $10^{1\frac{2}{3}}$ and 10^{2} Hz.

The spectral energy below 2 Hz is very homogeneous over the field, Figures 2a-c, but above 2 Hz the energy is stronger near the platform constructions in the center and south ends of the array, particularly visible in Figure 2f.

Frequency spectra as function of time

The spectrum is not constant over time, however, and to investigate its behavior we select all stations in a radius of 1.75 km centered at $(522, 6242)$ km. This location was selected after observing in Figure 2 that the spectrum is not dominated by platform-generated noise. All data in the four data sets were divided into 2.5-minute windows with 50% overlap, and the time-frequency spectrum was computed for each time-window and averaged over all selected stations. The spectrum is then shown in Figure 3 as a function of the center of each 2.5 minute window.

Observe how the spectrum varies for the different recordings; this reflects both the filter settings and transient nature of the ambient field over long periods. Furthermore, the spectrum is not constant during each recording. Notice, in Figure 3d above 10 Hz, the episodic nature of the seismic-survey shooting happening to the north-west of Valhall. When recording for long enough periods, the low frequency microseism noise in frequencies below 2 Hz can be seen to vary considerably over time (Figures 3c and 3d).

beam forming experiments

Because the station spacing is approximately 150 m between the cables and approximately 50 m between stations along the cable, the surface waves are aliased for all but the lowest of frequencies. We select all stations in a radius of 1 km centered at $(526.5, 6236.4)$ km and bandpass the data with a frequency domain Hann taper between $0.45 - 0.65$ Hz. Beam forming was conducted after slant stacking and averaging the absolute value of the $\tau - p$ domain over 30-minute time windows under a time domain Hann taper. Figures 4 to 7 contain beam forming experiments for all four data sets.

Beam forming of all data sets shows how the microseism noise is generally incident

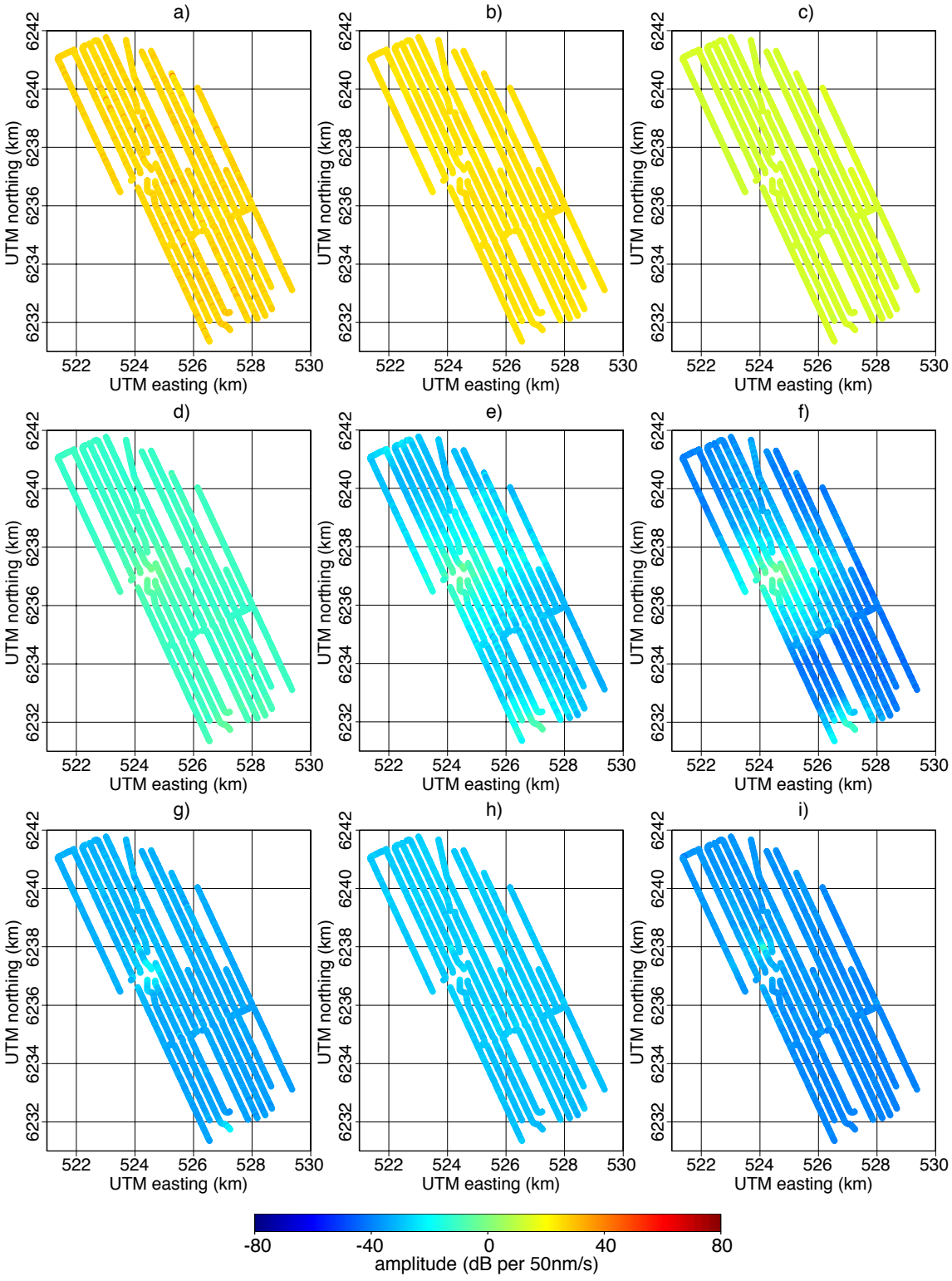

Figure 2: Spectra from data in December 2010. a) $10^{-\frac{2}{3}}$ Hz, b) $10^{-\frac{1}{3}}$ Hz, c) 10^{0} Hz, d) $10^{\frac{1}{3}}$ Hz, e) $10^{\frac{2}{3}}$ Hz, f) 10^{1} Hz, g) $10^{1\frac{1}{3}}$ Hz, h) $10^{1\frac{2}{3}}$ Hz, i) 10^{2} Hz. [**CR**]

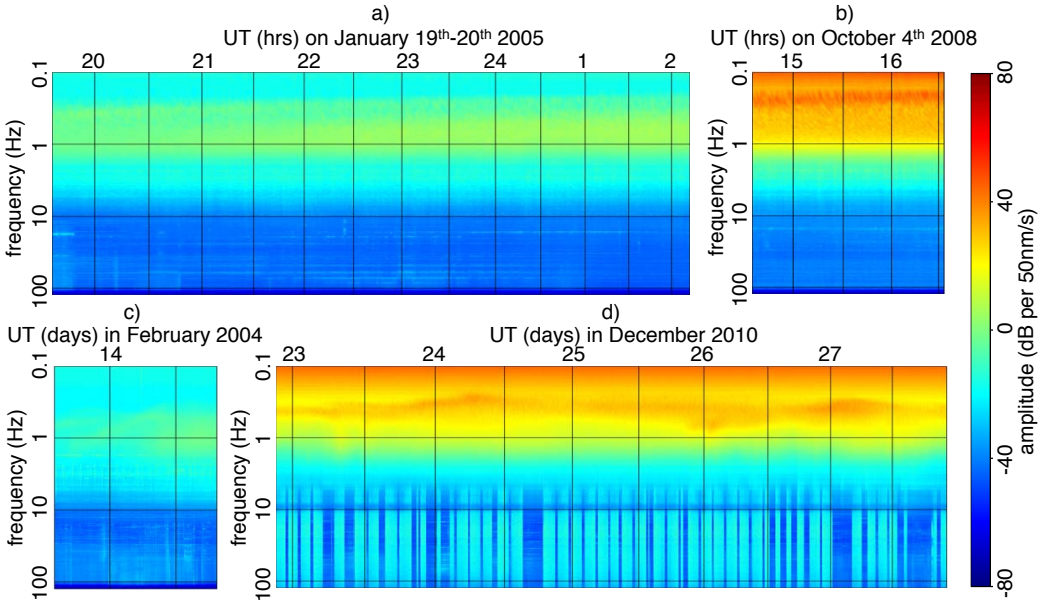

Figure 3: Spectragrams of vertical component of particle velocity for four different continuous passive recordings. a) 6 hours, 39 minutes and 30 seconds starting UT 19:35:45 on January 19$^{\text{th}}$ 2005, b) 2 hours starting UT 14:11:24 on October 4$^{\text{th}}$ 2008, c) 29 hours, 29 minutes and 16 seconds starting UT 14:14:14 on February 13$^{\text{th}}$ 2004, d) 5 days, 1 hour, 47 minutes and 20 seconds starting UT 21:16:39 on 22$^{\text{nd}}$ December 2010. [**CR**]

equally strongly with direction for long periods of time. In Figure 4 the microseism energy slowly, but continuously, increases in strength. This is not a diurnal cycle, because the 2004 data set spans more then 24 hours. The observation that microseism noise does not necessarily reflect diurnal cycles is corroborated by Figure 3c.

Figure 5 shows that for the 6 hours recorded in 2005, the microseism energy is remarkably homogeneous in direction (more so then for the other 3 data sets). This contributed to the successes achieved by Mordret et al. (2013a,b) in his studies of this data set. Figure 7 shows that over the course of 5 days, the microseism exhibited periods during which the noise came in particularly strongly from certain directions (Figure 7g), while during other periods there was no single direction standing out. Studying the beam forming results carefully, one observes an inner ring at a slowness corresponding to a velocity of about 2 km/s, and exhibiting an aliasing pattern spaced closer than the alias ring of the dominant mode (the alias can be observed in the corners of Figure 7b). This could be a manifestation of a higher mode traveling faster then the fundamental mode.

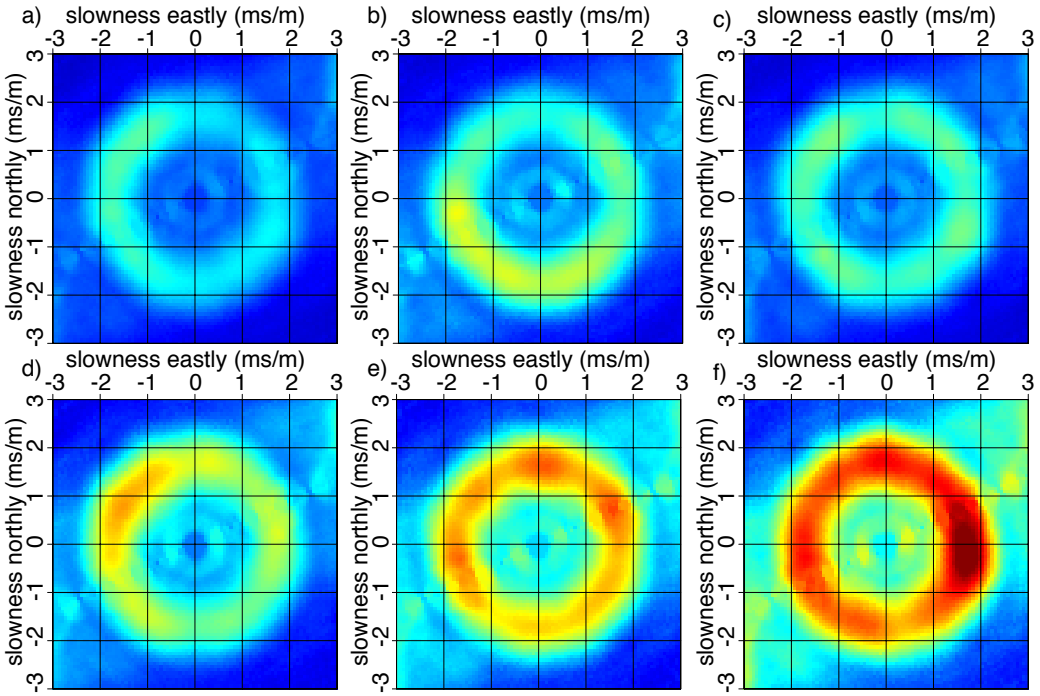

Figure 4: Beam forming for half-hour windows in February 13$^{\text{th}}$ 2004; centered around a) 16:00, b) 20:00 and half-hour windows in February 14$^{\text{th}}$ 2004, centered around c) 0:00, d) 4:00, e) 8:00, f) 12:00. [**CR**]

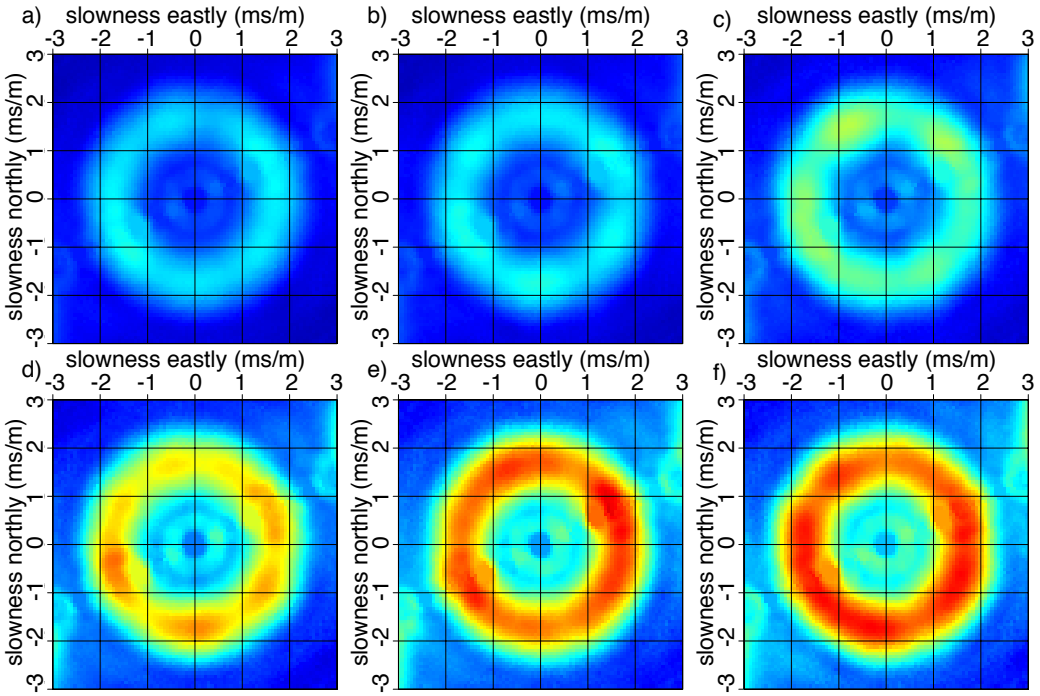

Figure 5: Beam forming for half-hour windows in January 19$^{\text{th}}$ 2005; centered around a) 20:00, b) 21:00, c) 22:00 d) 23:00 and half-hour windows in January 20$^{\text{th}}$ 2005, centered around c) 1:00, d) 2:00 [**CR**]

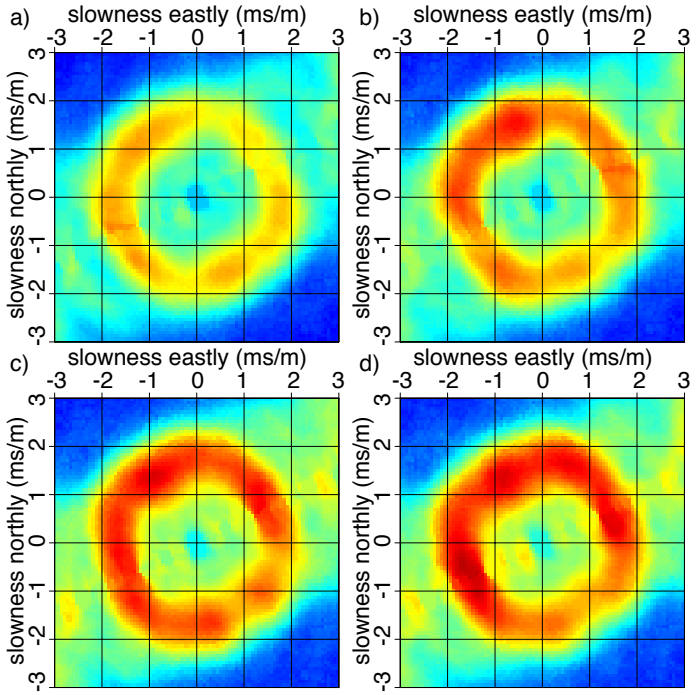

Figure 6: Beam forming for half-hour windows in October 4$^{\text{th}}$ 2008, half hours are centered around; a) 14:30, b) 15:00, c) 15:30, d) 16:00. [**CR**]

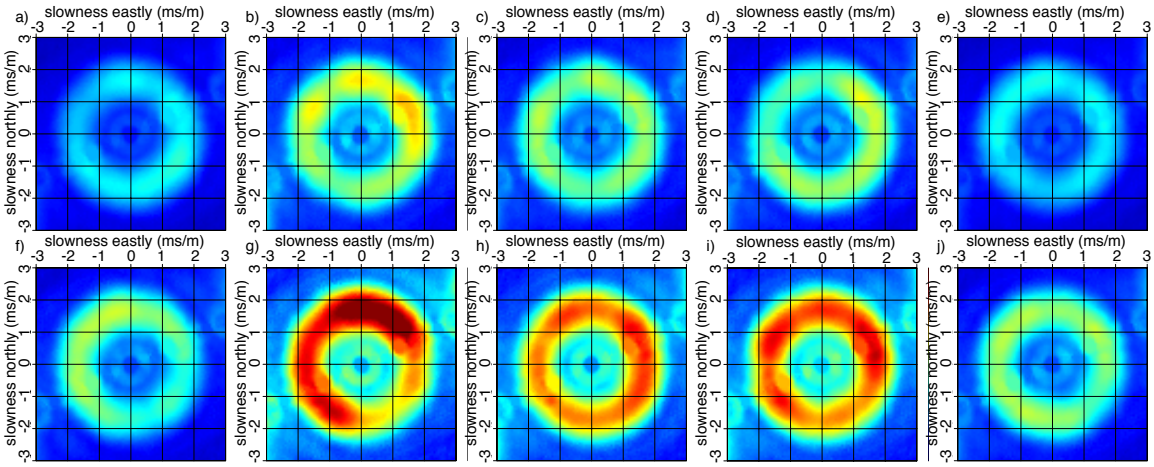

Figure 7: Beam forming for half-hour windows centered around a) 0:00 and b) 12:00 on December 23$^{\text{rd}}$, c) 0:00 and d) 12:00 on December 24$^{\text{nd}}$, e) 0:00 and f) 12:00 on December 25$^{\text{th}}$, g) 0:00 and h) 12:00 on December 26$^{\text{th}}$, i) 0:00 and j) 12:00 on December 27$^{\text{th}}$. [**CR**]

CORRELATION METHODOLOGY

Passive seismic interferometry is a technique that cross-correlates seismic recordings at two stations to form a signal, an estimated Green's function (EGF), as if one of the stations were a seismic source (Wapenaar and Fokkema, 2006). Cross-correlations of passive seismic recordings between all possible station pairs in an array then creates a full virtual seismic survey, $\mathbf{D}(\omega, x_r, x_s)$:

$$\mathbf{D}(\omega, x_r, x_s) = \mathbf{r}(\omega, x_r)\ \mathbf{r}(\omega, x_s)^{\dagger}, \tag{1}$$

where $\mathbf{r}(\omega, x)$ is a vector containing passive seismic recordings at all stations, and $\dagger$ denotes complex conjugation and transposition. By cross-correlating different components of particle velocity we can retrieve all elements of the Green's matrix (Wapenaar and Fokkema, 2006). However, this technique is valid only when the energy in the ambient seismic field satisfies a condition known as energy equipartioning. In practice, this requirement limits the application of seismic interferometry to certain frequency regimes. The ambient seismic field at low frequencies ($0.18 - 1.75$ Hz) is dominated by the double-frequency microseism peak, a source of seismic energy that satisfies the requirement of energy equipartitioning and can be utilized for seismic interferometry (Stewart, 2006; Dellinger and Yu, 2009). The LOFS array has geophone stations that consist of one in-line (with the cable) component and two perpendicular (to the cable) components. Station orientations were estimated from active seismic and provided with the data by BP. Using the orientations, the recordings are rotated to a vertical, east ,and north component. The recorded data in all three components (north, east, and vertical) of particle velocity was bandpass filtered using a frequency domain taper with a flat response for 0.2-1.5 Hz, and as a Hann-taper extending from 0.175 Hz to 1.75 Hz. The data was then divided into 30-minute segments with 50% overlap. For each segment, all stations and all components were cross-correlated. The resulting cross-correlations were stacked for all 30-minute segments, resulting in virtual seismic source and receiver matrices between all stations.

Figure 8 contains an example of a virtual seismic source in vertical particle velocity, located near the center of the array. This example was generated using all data in the 2010 recording. Each frame is a snapshot corresponding to a certain correlation-time lag; negative time lags correspond to the acausal EGF, while positive time lags correspond to the causal EGF. Note the good retrieval of both causal and anti-causal EGF's, without imposing symmetry conditions. This is due to the azimuthal homogeneity of the directions in the ambient seismic field as observed in the beam forming experiments in Figure 7.

Rotation NEV to RTV

A coordinate system based on north, east and vertical components is not the most natural coordinate system to study the EGF matrices. In a perfectly stratified media, the surface wave modes split into Love and Rayleigh-Scholte wave modes. Love

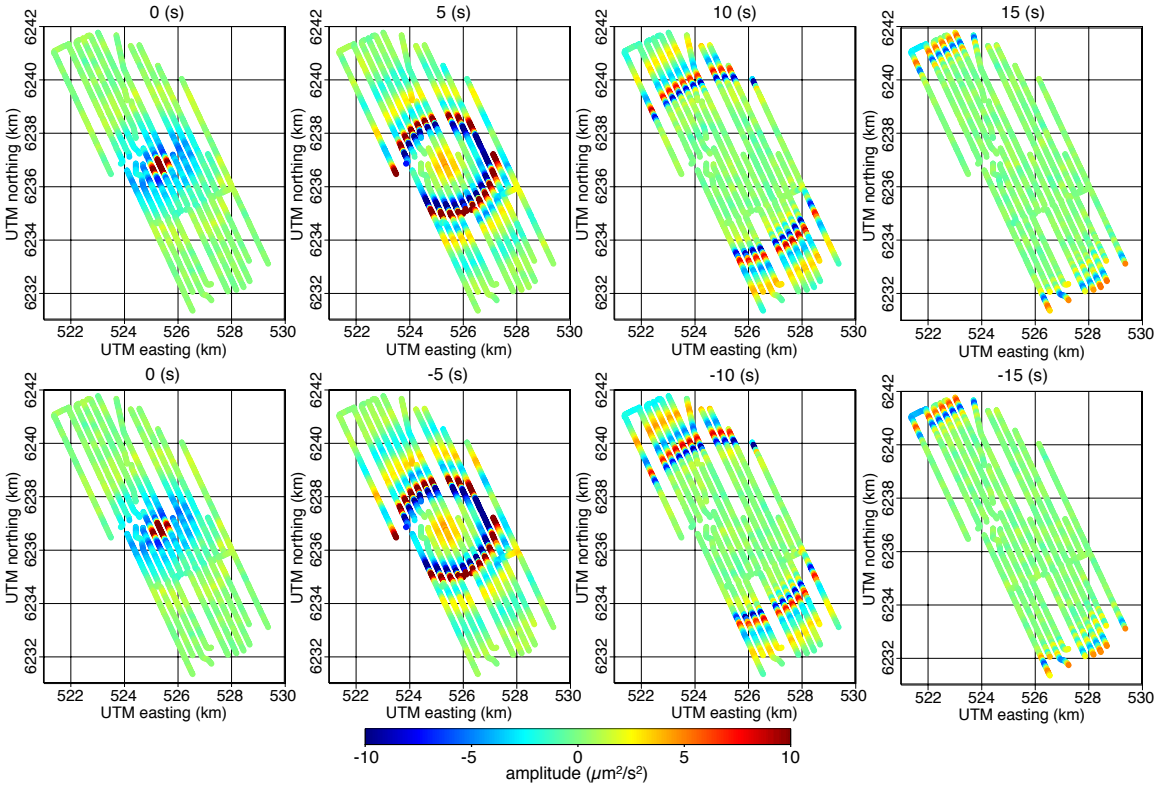

Figure 8: A virtual seismic source generated by processing all of the 2010 recording. The top row corresponds to positive correlation-time lags. The bottom row contains the corresponding negative correlation-time lags. [**CR**]

waves have transverse polarization and only appear in the transverse components, and Scholte wave appear in the vertical and radial components. Although we know that the subsurface at Valhall is anisotropic, and there are strong lateral inhomogeneities (Barkved and Kristiansen, 2005; Sirgue et al., 2010), these effects are secondary and the virtual seismic sources will, to first order, consist of Love and Scholte wave modes.

We exploit this first order behavior and rotate each virtual seismic source to a cylindrical coordinate system centered around the source. Thus all virtual seismic source matrices were transformed from a coordinate system with north, east, and vertical components, to a cylindrical coordinate system centered at the source station, with radial, tangential, and vertical components. The result of this transformation is shown in Figure 9. The left-group in Figure 9 shows time-slices of G_{nn}, G_{en}, G_{vn}, G_{ee}, G_{ve} and G_{vv} before rotation, while the right-group in Figure 9 shows the same time-slices after rotation into G_{rr}, G_{rt}, G_{rv}, G_{tt}, G_{tv} and G_{vv}. After this rotation, the polarity and amplitude of the EGF's should no longer depend on geographic direction. Directionality of the virtual seismic sources can however still caused by the directionality of the energy in the ambient seismic field and by subsurface lateral inhomogeneities.

Notice, in Figure 9, how the polarity of the observed wave front changes with azimuth for the various elements of the EGF matrix: In the G_{vv}, G_{nn} and G_{ee} elements the polarity is equal in all azimuths from the source, but the G_{nn} and G_{ee} elements are relatively weak in the east-west and north-south directions from the source, respectively. In the G_{vn} and G_{ve} elements the polarity flips in the north-south and east-west directions, respectively. In addition, G_{en} displays a butterfly pattern of flipped polarities and weak radiation. After rotation, the G_{vv} element remains the same. The G_{tt}, G_{rr} and G_{rv} elements are now radiating with equal polarity and more or less equal strength in all directions from the source. The G_{vv}, G_{vr} and G_{rr} elements are dominated by Scholte waves and the G_{tt} element is dominated by Love waves, while the G_{rt} and G_{tv}, expected to be zero in a perfectly stratified medium, display a complicated mixture of converted wave modes. Notice how the amplitudes in the G_{rr} G_{tt} and G_{rt} element are relatively weak, while the amplitude in the G_{tv} element is still relatively strong, because the ambient noise field is stronger in the vertical component then in the horizontal components.

W-P spectra

This virtual seismic survey was next transformed to a midpoint and radial-offset domain, and all offsets were selected for a group of midpoints in the southern part of the array. Dispersion images (Figure 10) are calculated as the amplitude in the Radon $(\omega - p)$ domain, balanced over frequencies. In the vertical-vertical, radial-radial and radial-vertical elements, these waves are dominated by fundamental-mode Scholte waves. The first overtone is also distinguishable and is more evident in the radial-radial than in the vertical-vertical element. The transverse-transverse element is dominated by Love waves that travel at a higher velocity (lower slowness) than

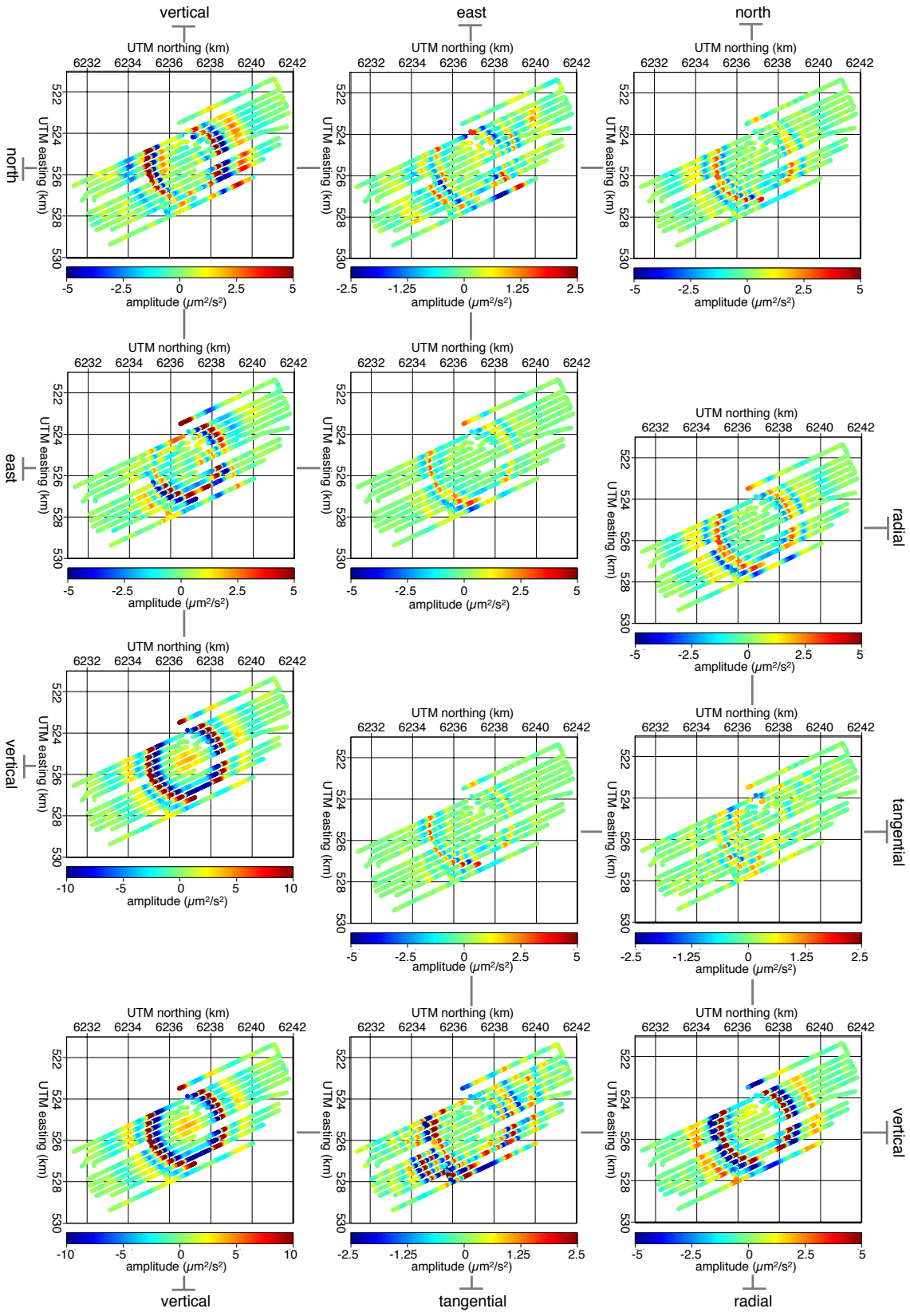

Figure 9: Time slices of virtual seismic source. [**CR**]

the fundamental-mode Scholte waves. The transverse-vertical and transverse-radial components are much weaker than the other elements (before normalization) and do not contain well-defined modes.

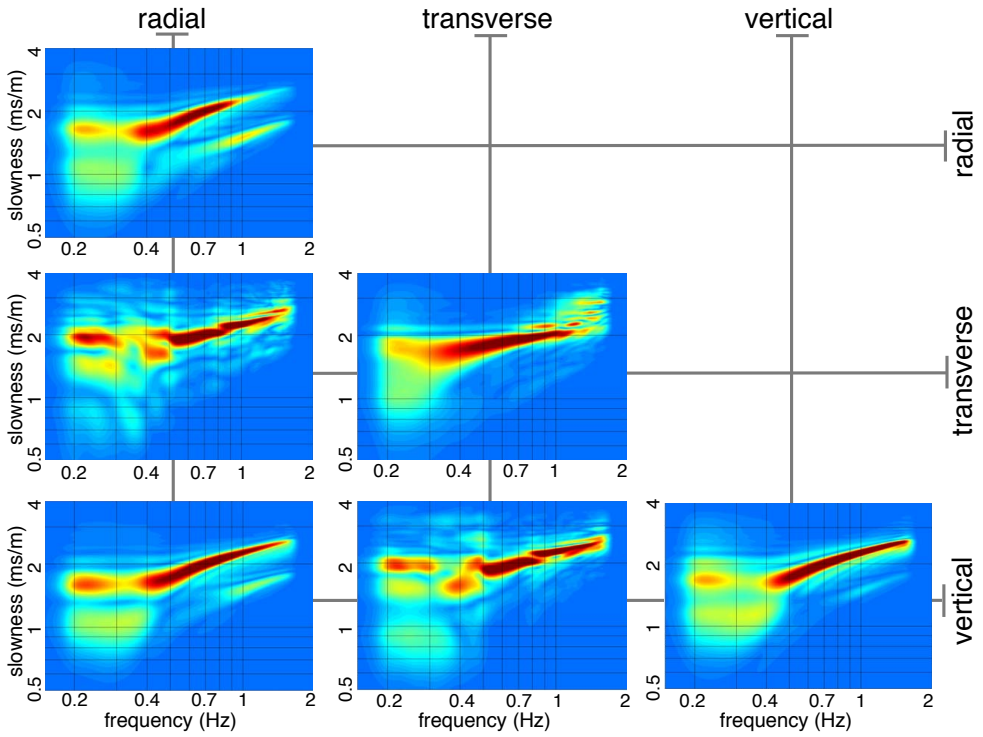

Figure 10: Dispersion images for all elements of the virtual seismic source matrix. [**CR**]

CONCLUSIONS

Strong microseism energy, although varying in strength over time, is present in the vertical component of the geophones for all four LOFS recordings. The low frequency microseism energy is best recorded with the low-cut recording filter (standard for active seismic acquisitions) turned off. At Valhall, the microseism energy is generally omnidirectional, but there are time periods that are an exception. Seismic interferometry is successfully applied using all components of geophones to create a virtual seismic Green's matrix. This matrix has to be rotated to a coordinate system with radial, tangential and vertical components with respect to the source-receiver couple in order to be well interpreted. The vertical-vertical, radial-radial, and radial-vertical components are dominated by fundamental mode Scholte waves. A first overtone is visible as well, more strongly in the radial-radial component then vertical-vertical component. The tangential-tangential component is dominated by Love waves traveling faster then Scholte waves. These waves, extracted with seismic interferometry, have wavelengths on the order of several hundred meters to several kilometers and provide sensitivity to the subsurface below the seafloor at Valhall.

ACKNOWLEDGEMENTS

Thanks to Olav Barkved, Biondo Biondi, Bob Clapp, Joe Dellinger, Jesse Lawrence, Stew Levin and Dave Nichols for helpful discussions and suggestions. Thanks to Adam Halpert for many comments and suggestions to this manuscript. Thanks to BP and the partners of the Valhall Field (BP Norge and Hess Norge) for permission to publish this paper. Thanks to the sponsors of the Stanford Exploration Project for financial support.

APPENDIX I

Fourier domain and spectra

Fourier transformations are powerful tools to analyses passive seismic recordings, not in the least because of their ability to characterize an infinitely long time series by a compact spectrum. We employ the following definition for the continuous-time Fourier transformation:

$$G(f) = \mathcal{F}_t \{g(t)\} = \int_{-\infty}^{\infty} \mathrm{e}^{-i2\pi ft} g(t) \mathrm{d}t, \tag{2}$$

and its inverse

$$g(t) = \mathcal{F}_t^{-1} \{G(f)\} = \int_{-\infty}^{\infty} \mathrm{e}^{i2\pi ft} G(f) \mathrm{d}f, \tag{3}$$

where $G(f)$ denotes the temporal Fourier domain counterpart of the function $g(t)$, t and f denote time and temporal frequency respectively. The temporal frequency f is regularly substituted by angular frequency $w = 2\pi f$. In practice we do not recording continuous and infinitely long time series, but instead record a limited number of discrete samples. Conjunctly, the Fourier spectrum is not continuous; the discrete time-series is decomposed into a discrete number of Fourier coefficients. For a time series containing N samples with sampling Δt, the time and frequency are discretised as:

$$t \rightarrow \mathbf{f} = t_n = n\Delta f \quad \text{with} \;\; n = -N/2, -N/2+1, ..., N/2-1, \tag{4}$$

$$f \rightarrow \mathbf{f} = f_m = m\Delta f \quad \text{with} \;\; m = -N/2, -N/2+1, ..., N/2-1, \tag{5}$$

where the frequency sampling, Δf, is related to N and Δt as shown below. The continuous time and frequency functions $g(t)$ and $G(f)$ are consequently discretised as

$$g(t) \rightarrow \mathbf{g}(t_n) \quad \text{with} \;\; n = -N/2, -N/2+1, ..., N/2-1, \tag{6}$$

$$G(f) \rightarrow \mathbf{G}(f_m) \quad \text{with} \;\; m = -N/2, -N/2+1, ..., N/2-1. \tag{7}$$

Substituting these into the definition of the forward and inverse Fourier transformation, Equations 2 and 3, we find

$$\mathbf{G}(f_m) = \sum_{n=-N/2}^{N/2-1} \mathbf{g}(t_n) e^{-i2\pi(\Delta t \Delta f \ n \ m)} \Delta t, \tag{8}$$

$$\mathbf{g}(t_n) = \sum_{m=-N/2}^{N/2-1} \mathbf{G}(f_m) e^{i2\pi(\Delta t \Delta f \ n \ m)} \Delta f. \tag{9}$$

Notice that the periodicity of the Fourier kernel relates Δt, Δt and N as:

$$N \Delta f \Delta t = 1 \tag{10}$$

Although Equations 8 and 9 are the discrete versions of Equations 2 and 3, more modifications are needed to be find the Discrete Fourier transformations as commonly applied by packaged such as FFTW. First, replace the negative counters with $n \rightarrow n+N$ and $m \rightarrow m+N$ to rearrange the summations to run over positive indices only. The summations now run from 0 to 2π instead of from π to π. As a consequence the DFT algorithms expect first all the positive time-lags and then all the negative time-lags, and a similar rearrangement of the frequency axis. Secondly, scale the variable G_m by Δt and substitute the factor $\Delta f \Delta t$ with $1/N$, now the DFT algorithm operates independently of Δt and Δt while maintaining invertability. Finally we have:

$$\mathbf{G}(f_m) = \sum_{n=0}^{N-1} \mathbf{g}(t_n) e^{-i2\pi \frac{n \ m}{N}}, \tag{11}$$

$$\mathbf{g}(t_n) = \frac{1}{N} \sum_{m=0}^{N-1} \mathbf{G}(f_m) e^{-i2\pi \frac{n \ m}{N}}. \tag{12}$$

If we which to find the discrete version of the continuous Fourier transformations as defined in Equations 2 and 3 using the FFTW package, we need to scale the outcome of the forward transformation by Δt and that of the inverse transformation by $\frac{1}{\Delta t}$.

After Fourier transformation, a time-series can be characterized by its amplitude and phase spectra of the complex Fourier coefficients. And the energy in a time-series is characterized by the power spectrum. If a time series of length $N\Delta t = T$, measures an electrical voltage in V, the application of the Discrete Fourier transformation, Equation 8, transforms the unit into V. The amplitude spectrum now corresponds to the amplitudes of the time domain sinusoidal basis functions that are used to decompose the time series. For time-series that are purely real, the symmetry of the resulting Fourier domain spectrum can be exploited by multiplying the amplitude spectrum by two and analyzing the spectrum for positive frequencies only. Thus the amplitude spectrum is defined by:

$$\mathbf{S}(f_m) = 2\,|\mathbf{G}(f_m)| \quad \text{with} \quad m = 0, 1, ..., N/2 - 1 \tag{13}$$

The power spectrum is defined as the square of the Fourier spectrum:

$$\mathbf{P}(f_m) = 2\left(\mathbf{G}(f_m)\mathbf{G}(f_m)\right) \text{with} \;\; m = 0, 1, ..., N/2 - 1 \tag{14}$$

It represents the energy in signal normalized per $T(s)$ used for the DFT. The units of amplitude are now in V^2.Finally Parceval's theorem will require

$$\Delta t \sum_{n=-N/2}^{N/2-1} \mathbf{g}(t_n) = \Delta f \sum_{n=-N/2}^{N/2-1} \mathbf{G}(f_m) \text{with} \;\; n = 0, 1, ..., N/2 - 1 \tag{15}$$

which validates if the scaling was performed correctly.

Amplitude and power spectra have a large dynamic range and are therefore often studied on a logarithmic scale with a reference variable. For a power spectrum we define a decibel as:

$$\mathbf{P}(f_m)[dB] = 10\text{Log}_{10}\left(\frac{\mathbf{P}(f_m)[nm/s]}{\alpha_{ref}}\right). \tag{16}$$

For an amplitude spectrum we define a decibel as

$$\mathbf{S}(f_m)[dB] = 10\text{Log}_{10}\left(\frac{\mathbf{S}^2(f_m)[nm/s]}{\alpha_{ref}^2}\right) = 20\text{Log}_{10}\left(\frac{\mathbf{S}(f_m)[nm/s]}{\alpha_{ref}}\right) \tag{17}$$

where the factor 20 derives from the square to keep decibel levels similar for amplitude and power spectra. The unit is typically denoted as (dB re $1\alpha_{ref}$), where α_{ref} is the reference level. Standard reference levels for pressure in are $p_{ref} = 20[\mu Pa]$ (in air) and $p_{ref} = 1[\mu Pa]$ (under water) and for particle velocity $v_{ref} = 50[nm/s]$.

Instead of looking at the power spectrum of one signal we could study the cross-spectrum between two signals, $\mathbf{G}$ and $\mathbf{H}$:

$$\mathbf{C}(f_m) = 2\left(\mathbf{G}(f_m)\mathbf{H}(f_m)\right) \tag{18}$$

After inverse Fourier domain this yields a cross-correlation function, which is best normalized by time to be insensitive to the amount of time cross-correlated). The unit of this cross-correlation signal is now V^2.

Finally we employ the following definition for the spatial Fourier transformation:

$$G(\xi) = \mathcal{F}_x\left\{g(x)\right\} = \int_{-\infty}^{\infty} \mathrm{e}^{i2\pi\xi x} g(x)\mathrm{d}x, \tag{19}$$

and its inverse

$$g(x) = \mathcal{F}_t^{-1}\left\{G(x)\right\} = \int_{-\infty}^{\infty} \mathrm{e}^{-i2\pi\xi x} G(x)\mathrm{d}\xi. \tag{20}$$

The spatial frequency ξ is regularly substituted by the wave number $k = 2\pi\xi$. Equations 19 and 20 are discretised similarly as Equations 19 and 20.

REFERENCES

Artman, B., 2006, Imaging passive seismic data: Geophysics, **71**, SI177–SI187.

Barkved, O. I., and T. Kristiansen, 2005, Seismic time-lapse effects and stress changes: Examples from a compacting reservoir: The Leading Edge, **24**, 1244–1248.

Dellinger, J., 2008, Low frequencies using conventional sensors: "sign-bit" recording revisited: SEG Technical Program Expanded Abstracts, **27**, 149–153.

Dellinger, J. A., and J. Yu, 2009, Low-frequency virtual point-source interferometry using conventional sensors: 71st Meeting, European Associated of Geoscientists and Engineers, Expanded Abstracts, X047.

McNamara, D., and R. Boaz, 2005, Seismic noise analysis system using power spectral density probability density functions: A stand-alone software package: USGS Open-File Report, 1–14.

Mordret, A., M. Lands, N. M. Shapiro, S. C. Singh, P. Roux, and O. I. Barkved, 2013a, Near-surface study at the valhall oil field from ambient noise surface wave tomography: Geophysical Journal International.

Mordret, A., N. M. Shapiro, S. Singh, . Roux, J. P. Montagner, and O. I. Barkved, 2013b, Azimuthal anisotropy at valhall: the helmholtz equation approach: Geophys. Res. Let.

Sirgue, L., O. I. Barkved, J. Dellinger, J. E. U. Albertin, and J. H. Kommedal, 2010, Full waveform inversion: the next leap forward in imaging at Valhall: First Break, **28**, 65–70.

Stewart, P., 2006, Interferometric imaging of ocean bottom noise: SEG Technical Program Expanded Abstracts, **25**, 1555–1559.

Wapenaar, K., 2004, Retrieving the elastodynamic Green's function of an arbitrary inhomogeneous medium by cross correlation: Phys. Rev. Lett., **93**, 254301–1 – 254301–4.

Wapenaar, K., and J. Fokkema, 2006, Green's function representations for seismic interferometry: Geophysics, **71**, SI33–SI46.